

Image distortion and correction in single photon emission CT

Koichi OGAWA

Department of Electronic Informatics, Faculty of Engineering, Hosei University

The task of single photon emission CT (SPECT) is to visualize the physiological function of various organs with the help of radiopharmaceuticals. But the projection data used for image reconstruction are distorted by several factors, making the reconstruction of a quantitative SPECT image very difficult in most cases. These factors include the attenuation and scattering of gamma rays, collimator aperture, data acquisition method, movement of organs, and washout of radiopharmaceuticals. This review article classifies the causes of the distortion in SPECT images and describes correction methods.

Key words: single photon emission CT, image distortion, correction, image processing

1. INTRODUCTION

SINGLE PHOTON EMISSION CT (SPECT),^{1–9} which can measure functions of internal organs as an image, is an important technology in present-day medicine. But there are several difficulties involved in obtaining a quantitative image in SPECT.^{10–14} The causes of image distortions in SPECT can be divided roughly into the following four groups. The first group relates to the interactions of gamma rays with internal organs, and I have named this group “physical factors.” The second relates to data acquisition equipment or data acquisition protocols, which I have named “measurement system factors.” The third relates to the image reconstruction method, which I have named “image reconstruction factors.” And the last one relates to physiological factors, which I have named “physiological factors.” The influence of the above factors on the quality of a reconstructed image is described in section 2, and the correction methods for the major distortion factors (attenuation, scattering and collimator aperture) are described in sections 3–5.

2. IMAGE DISTORTIONS

2.1 Physical factors

In nuclear medicine physiological functions of various organs are imaged with detected gamma rays being emitted from radiopharmaceuticals accumulated in a targeted organ. These gamma rays interact with various atoms that constitute the human body. The interactions include incoherent scattering (Compton scattering), photoelectric absorption and coherent scattering, because the photo-peak energies of radionuclides used in SPECT range from 71 keV (²⁰¹Tl) to 300 keV (⁶⁷Ga). These relatively low-energy gamma rays commonly interact, in Compton scattering, with atoms which constitute the bones or soft tissues. Compton scattering is an elastic collision of a gamma ray with an orbital electron of an atom. The gamma ray gives a part of its energy to the orbital electron, and the atom emits this orbital electron as a recoiled electron. After this collision, the gamma ray (scattered photon) changes its direction of travel according to the rules of preservation of energy and momentum. In this collision the energy of the scattered photon decreases, because the scattered photon gives its own energy to the orbital electron. Some of the scattered photons disappear due to photoelectric absorption after Compton scatterings in the body. And some of the scattered photons leave the body. As a result, the number of photons passing through collimator holes and measurable with a gamma camera becomes very small. The photoelectric absorption is the second probable interaction between gamma rays and

Received January 8, 2004, revision accepted January 27, 2004.

For reprint contact: Koichi Ogawa, Ph.D., Department of Electronic Informatics, Faculty of Engineering, Hosei University, 3–7–2 Kajinocho, Koganei, Tokyo 184–8584, JAPAN.

E-mail: ogawa@k.hosei.ac.jp

atoms. In this interaction all the energy of a gamma ray is deposited on the atom causing the interaction, and the photon disappears. When the photoelectric absorption occurs, the atom emits the orbital electron obtaining the energy of the gamma ray as a photoelectron; then this photoelectron loses its kinetic energy and becomes a free electron nearby. The probability of photoelectric absorption in the human body is high when the energy of a photon is less than about 50 keV. And the lower the energy of the photon, the higher becomes the probability of the interaction. The third one is coherent scattering, in which the energy of a gamma ray does not change, but the direction of travel changes slightly. Because the atomic numbers of atoms which constitute the human body are very low, this probability is high only when the energy of the gamma ray is very low. Thus coherent scattering can be ignored in most examinations in nuclear medicine. The above two interactions (Compton scattering and photoelectric absorption) therefore seriously affect the projection data in SPECT. When Compton scattering occurs, the number of photons that should be measured ideally decreases, and there seems to be little source on the strip area passing through a collimator hole. Moreover, the number of detected photons decreases, because some of the gamma rays disappear due to photoelectric absorption. The attenuation of the gamma ray means these two phenomena, and this attenuation causes low frequency distortion in a reconstructed image. On the other hand, when Compton scattering occurs and the energy of a scattered photon is within the range of the energy window, the scattered photon is measured as if it was a primary photon. The scattering of gamma rays means this phenomenon, and the number of detected photons is increased by these scattered photons. In this case, the low frequency components of a reconstructed image increase and the contrast in this image decreases. In dual-radionuclide studies the problem originating in scattered photon causes serious distortion in a reconstructed image. Beside the above physical factors, detected gamma-ray counts inherently have statistical noise. This is the phenomenon in which the number of photons measured in unit period changes statistically. That is, the number of observable events changes according to the Poisson distribution, and the measured counts are distributed around the expected value. When a large statistical noise exists in the projection data, checkerboard patterns appear on the reconstructed images.

2.2 Measurement system factors

Because a single photon emitter is used in SPECT study, a collimator is required to restrict the traveling direction of gamma rays in data acquisition. This collimator causes distortions in a reconstructed image. In general, gamma rays passing through a collimator hole are not only the photons which enter the hole parallel to its axis, but also those which enter the hole at an acute angle to the hole

axis. This angle depends on the diameter and length of the hole, and due to this angle the original location of a measured photon cannot be restricted to a strip area parallel to the hole axis of the collimator. This is contrary to the assumption used in the Radon transform, that is, a projection is an integration of given physical values in a straight line. As a result, shift-variant blurring occurs, and the influence of blurring depends on the distance between source positions and the collimator surface. In the data measurement process another image distortion sometimes occurs, depending on the way projection data are measured. For example, the stationary (step-and-shoot mode) and dynamic (continuous mode) data acquisition methods change the spatial resolution of a reconstructed image. As for the data acquisition area, there are 180- and 360-degree data acquisition methods¹⁵⁻²⁰ in myocardial SPECT. The 180-degree data acquisition generates low frequency distortion and artifacts in the base of the myocardium, even though the projection data have good signal-to-noise ratios and the data acquisition time is short. The image quality of the left ventricle is superior to the images reconstructed with the 360-degree projection data. On the other hand, as for the quality of reconstructed images, the low frequency distortion is smaller than that of the 180-degree data acquisition because of the averaging effect of the projection data. But the 360-degree data acquisition has a drawback in that the statistical noise in the projection data becomes predominant in angles where the heart is located far from the detector, and the data acquisition time is longer than that of the 180-degree data acquisition. The image distortion originating in data acquisition also includes the non-uniform sensitivity of the gamma camera and misalignment in the rotational center of the detector.

2.3 Image reconstruction factors

Image distortion sometimes is generated due to the inappropriate use of the image reconstruction method. The filtered backprojection method or an iterative image reconstruction method is commonly used in commercially available data processing computers in nuclear medicine. The former is one of the typical analytical methods, and sometimes involves serious artifacts when the number of projections is inadequate or when there is a high uptake area within the image reconstruction slice. These artifacts are caused by a large negative or positive value due to high frequency components in filtered projection data. The latter methods include the maximum likelihood-expectation maximization (ML-EM) method²¹⁻²⁴ and the maximum a posterior-expectation maximization (MAP-EM) method.²⁵⁻²⁸ These are based on the statistical estimation theory. It takes a long time to obtain the last image with these methods, because of their slow convergence. So if one stops the calculation of image reconstruction at an inappropriate iteration time, distortion remains due to low frequency components in the reconstructed image. The

ordered-subset expectation maximization (OS-EM) method²⁹ or the block iterative image reconstruction method^{30,31} which decreases the calculation time required for image reconstruction sometimes increases the statistical noise with an inappropriate subset level, i.e., the number of projections in a subset. The subset level and number of iterations have to be carefully selected.^{32,33}

2.4 Physiological factors

Artifacts are generated when internal organs move during the acquisition of projection data. We cannot control the movement of the heart, so that a blurring occurs in the myocardial SPECT study. The movement of an organ with respiration may also generate serious artifacts on a reconstructed image.³⁴ This movement degrades not only the spatial resolution but also the contrast resolution, and makes it difficult to measure the physiological function of an organ quantitatively. In addition to the above problems, the variation of the distribution of the radiopharmaceuticals during the data acquisition causes an artifact when the speed of the metabolism of radiopharmaceuticals is faster than the data acquisition time.

3. ATTENUATION OF GAMMA RAYS

The attenuation of gamma rays is caused by photoelectric absorption and coherent/incoherent scattering, and this coefficient is called the linear attenuation coefficient μ (1/cm). μ is a function of the energy of a gamma ray and the material with which the gamma ray interacts. If the material is water, the linear attenuation coefficient becomes 0.19 (1/cm) for ²⁰¹Tl (71 keV) and 0.15 for ^{99m}Tc (140 keV). And the attenuation of the gamma ray obeys Beer's law. That is, the probability of the gamma ray which can transmit the water with x (cm) thickness becomes $\exp(-\mu x)$. For example, if we use ^{99m}Tc, the ratio of the gamma rays passing through the water with 5 cm thickness is 0.47. In the case of ²⁰¹Tl, photon energies are lower than those of ^{99m}Tc so that the ratio becomes 0.39. The human body is always supposed to be a water equivalent material, and so the influence is serious. Figure 1 shows the effect of attenuation on a reconstructed image. In this simulation we suppose a disc filled with water (^{99m}Tc solution) having uniform activity. In this figure absorbed photons cause a bowl-shaped artifact on a reconstructed image.

3.1 Attenuation correction methods

Attenuation correction is very important for reconstructing a quantitative SPECT image. Several attenuation correction methods have been proposed in the last three decades. In the 1970–1980s, simple methods which correct measured projection data or a reconstructed image were proposed.^{35–42} And in 1980–2000, analytical methods based on the inversion of the attenuated Radon transform^{43–48} and iterative methods were proposed.^{27,49–56}

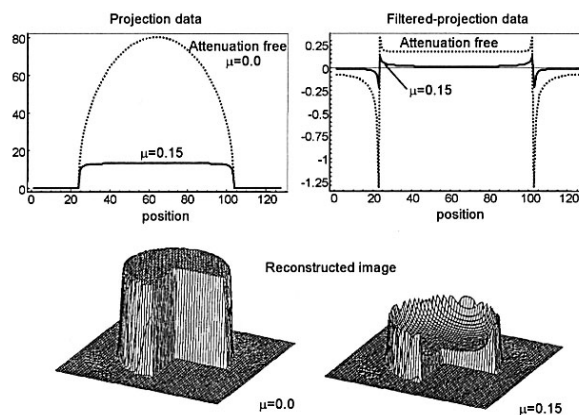


Fig. 1 Attenuated projection data and a reconstructed image (uniform activity: 1, radius of the cylinder: 8 cm ϕ). Projection data are affected by attenuation of gamma rays, and the image reconstructed with these distorted projection data generates a bowl-shaped artifact. In the reconstructed images a quarter part is cut in order to illustrate the profile of the image.

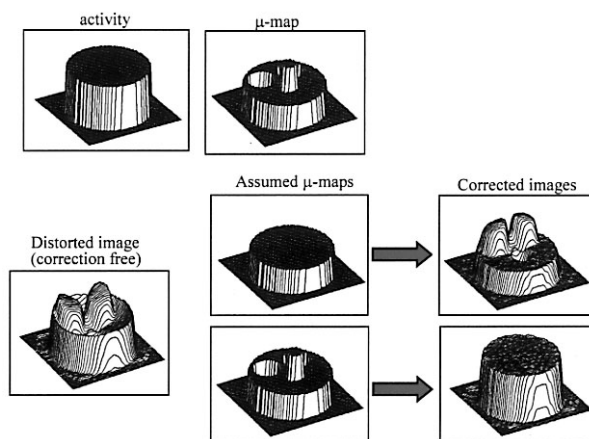


Fig. 2 μ -maps and corrected images. In this simulation attenuation correction is performed with Chang's method. The activity is uniformly distributed in the disc phantom, and the measured projection data are affected by the non-uniform attenuation effect shown in the μ -map (top). If we assume the μ -map to be uniform and correct the attenuation, the resultant image differs from the original one (middle). But if we know the actual μ -map, we can correct the effect of attenuation perfectly (bottom).

These attenuation correction methods are divided into two groups according to the distribution of the attenuation coefficient (μ -map); one assumes the distribution to be uniform and the other assumes it to be non-uniform. The former assumption makes it simple to compensate for the attenuation effect, but in most cases the supposed μ -map differs from the actual one, and serious artifacts occur in a corrected image due to the missetting of the distribution. For example, in a CBF SPECT study the attenuation coefficient is sometimes assumed to be uniform. But the thickness of the skull bone differs position-by-position,

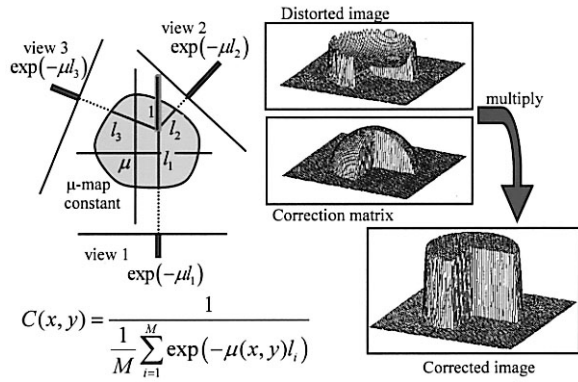


Fig. 3 The correction matrix is calculated from the attenuated projection data obtained with a phantom supposing unit activity. The correction factor, which is an element of the correction matrix, depends on the μ -map and the position of the element of interest. We multiply the distorted image by the correction matrix, and the compensation is performed in the iterative manner.

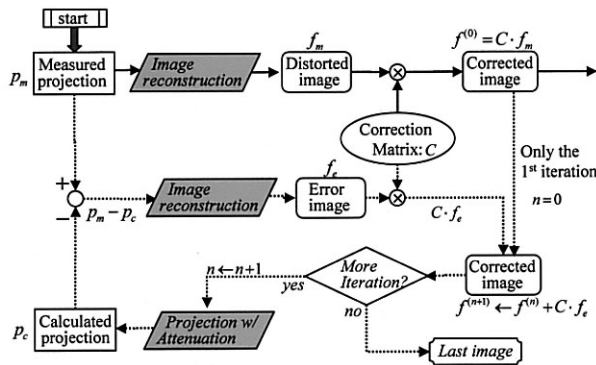


Fig. 4 Flow of correction procedure in Chang's method. Solid lines show the non-iterative correction process and dotted lines show the iterative correction process. In the iterative process an error projection is calculated and an error image being multiplied by the correction matrix is added to the latest compensated image.

and a supposed incorrect μ -map yields incorrect SPECT values. Figure 2 shows the importance of the true μ -map in attenuation correction. This figure shows that if we use a wrong μ -map in attenuation correction, the corrected SPECT image differs from the original one. Thus, an accurate μ -map is indispensable in attenuation correction, so that we describe here only the latter group which uses a true μ -map in attenuation correction.

One of the most popular attenuation correction methods is Chang's method.³⁹ In this method we first make a correction matrix $C(x, y)$ calculated with a μ -map and correct the distortion with this matrix at each iterative compensation step. This correction matrix consists of the correction factor at each pixel position, and this value is the inverse of the average probability of photons which originate in the pixel of interest, transmit the attenuator

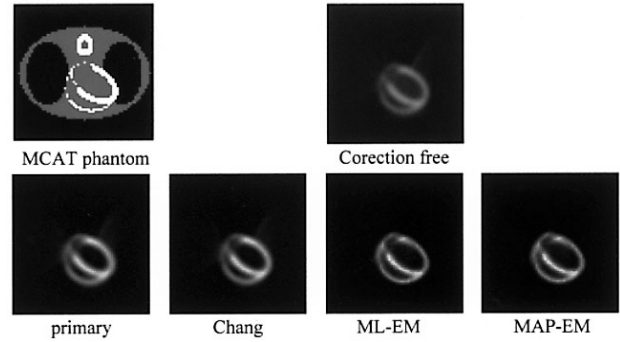


Fig. 5 Comparison of attenuation correction methods. In this simulation we use the MCAT phantom and set uniform activity at the myocardium. This μ -map includes different attenuation coefficients at bone, lungs and soft tissues. The image corrected with the true μ -map has almost the same quality.

and reach the detector (Fig. 3). The correction is done in the iterative manner shown in Figure 4. In each correction step we reconstruct an error image with error projections that are the difference between measured projection data and calculated projection data considering the attenuation effect described by the μ -map, and then multiply the error image by the correction matrix and add this to the latest compensated image. This method is applicable to an image distorted by both uniform and non-uniform attenuators. So if we can obtain a true μ -map, we can correct the distortion caused by attenuation for any object. This method has, however, the drawback of statistical noise.⁵⁷ When the count in projection data is inadequate, the iteration process strongly enhances the statistical noise. So we have to stop the correction process with only a few iterations even though the attenuation correction is not well accomplished.

The second popular method for attenuation correction is based on the statistical framework.^{27,55,56} There are two typical iterative methods for reconstructing an image, i.e., ML-EM and MAP-EM. Many researchers studied the ML-EM and MAP-EM methods in the 1990s. In these reconstruction methods we can easily introduce models of physical phenomena such as attenuation and scattering of gamma rays. The attenuation correction with ML-EM is performed by introducing a new term representing the attenuation effect in the reconstruction formula shown by Eq. (1):

$$\lambda_j^{n+1} = \lambda_j^n \frac{1}{\sum_{i \in J_j} c_{ij}} \sum_{i \in J_j} c_{ij} \frac{Y_i}{\sum_{k \in I_i} c_{ik} \lambda_k^n} \quad (1)$$

where J represents the number of pixels in a reconstructed image, and λ_j^n is the expected value of pixel j at iteration n . I is the number of detectors. Y_i is the projection measured with the i th detector. c_{ij} is the conditional probability of photons emitted by pixel j and detected at detector i . In order to introduce an attenuation term we replace λ_k^n in

Eq. (1) with λ_k^n multiplied by an exponential term in consideration of the phenomenon of attenuation. If the μ -map is already known, we can calculate an integral value of attenuation coefficients from a certain pixel to a detector position in a line perpendicular to the front surface of the detector, and accomplish the attenuation correction with the modified version of Eq. (1). Figure 5 shows reconstructed images of the myocardium (MCAT phantom)⁵⁶ corrected with a true μ -map. In this simulation projection data were calculated by a Monte Carlo simulation with 1 M photons (^{99m}Tc). The number of projections was 90, and the size of the image matrix was 64×64 . In Chang's method the number of iterations was two with a 3×3 spatial smoothing. In the ML-EM method and the MAP-EM method with a Gibbs prior, the number of iterations was 30. This figure shows that there is no significant difference among these correction methods if we can obtain a true μ -map.

The third approach is the analytical attenuation correction to the non-uniform attenuator. Research on analytical attenuation correction to a uniform attenuator was started by Bellini⁴³ in 1979 and completed by Metz and Pan⁴⁸ in 1995. Figure 6 shows the images corrected by Tretiak's method (C), Inoue's method (D), Bellini's method (E) and Metz's method (F). The attenuation coefficient is uniform inside the elliptical area (0.15 [1/cm]) and the projection data include statistical noise (total 100 k counts). The unified method⁴⁸ shows a good result under the existence of Poisson noise. Recently, Natterer⁵⁸ and Kunyanski⁵⁹ individually proposed an accurate, analytical attenuation correction method for a non-uniform attenuator. This work was completed by solving the Novikov inversion formula.¹²⁵ When attenuation is free, this Novikov inversion equation corresponds to the expression of the Radon inversion formula. In this correction process, normalized projection data are made from measured projection data and the divergent transform, which means the integral of attenuation coefficients from a given point, is multiplied by the above normalized projection data. Next, we differentiate these data on the axis of position of the projection data and backproject the data to a reconstructed image. These normalized projection data are composed of the Radon transform of the μ -map and the Hilbert transform of the Radon transformed value. After their excellent work, some modification methods were proposed.^{60,61,126,127} Figure 7 shows the image corrected by our program in which we implemented Kunyanski's formulation (C). The image (128×128) distorted by a non-uniform attenuator is corrected perfectly. The number of projections was 256 over 360 degrees. More work is necessary to clinically evaluate the above method.

3.2 How to get the μ -map

In section 3.1 we show the necessity of a μ -map in reconstructing a quantitative SPECT image. The methods for obtaining the μ -map can be divided roughly into three

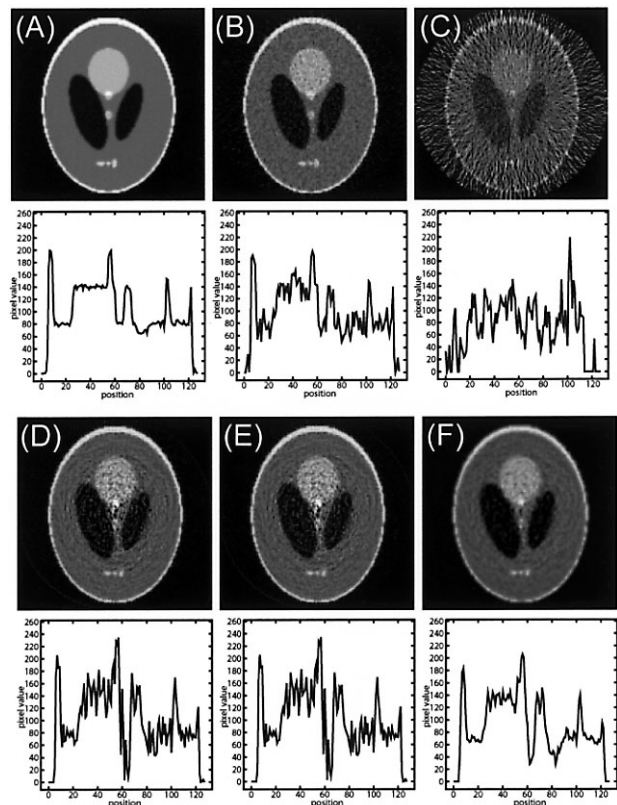


Fig. 6 Comparison of analytical attenuation correction methods. In this simulation we use the Shepp phantom (128×128) and calculate 128 projection data considering a μ -map with the uniform value (0.15 [1/cm]). (A) shows the image reconstructed with the filtered backprojection (FBP) method. Projection data have no attenuation or statistical noise. The profile is obtained at $x = 64$ (center). From (B) to (F) the projection data have statistical noise. (B) shows the image reconstructed with the FBP method (projection data have no attenuation). (C), (D), (E) and (F) are images corrected by Tretiak, Inoue, Bellini and Metz's methods, respectively.

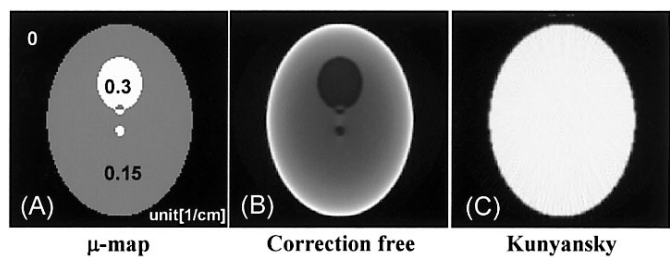


Fig. 7 Images corrected by the analytical attenuation correction methods for the non-uniform μ -map. The distribution of activity is uniform. (A) shows the non-uniform μ -map, (B) shows a reconstructed image by attenuated projection data. The image is distorted by the non-uniform attenuation. (C) shows a image corrected by an implementation proposed by Kunyanski.

groups.

The first group estimates the μ -map with the gamma ray emission CT data with the help of some restriction for the

distribution of attenuation coefficients.^{42,62,63} In this method we reconstruct the μ -map with the emission CT data iteratively under some constraint for the distributions of the attenuation coefficient. This is not always applicable to clinical studies.

The second one obtains the μ -map by a segmentation method.⁶⁴⁻⁶⁹ In order to obtain the shape of organs such as lungs, bones, liver and myocardium, we use images reconstructed with projections consisting of scattered photons, images reconstructed by an MRI scanner or transmission CT images reconstructed with projections measured by an external gamma ray source. After the shapes (regions) of the organs are fixed by a segmentation method, predefined attenuation coefficients are set to regions representing the organs. The attenuation coefficients in the μ -map do not always agree with actual values, and the shape obtained by the segmentation method may sometimes be inaccurate, precluding the frequent use of this method in clinical studies.

The third one uses the μ -map directly measured by gamma-ray transmission CT (TCT)^{57,70-81} or X-ray CT.⁸²⁻⁸⁶ The advantages of using gamma ray TCT are as follows: 1) the μ -map can be measured with gamma rays having the single photo-peak energy, 2) the TCT and emission CT (ECT) data can be acquired simultaneously or sequentially by means of the same modality. Gamma ray TCT is superior to X-ray CT, because the X-ray is polychromatic and the attenuation coefficient depends on the photon energy. The method with gamma ray TCT enables us to avoid misregistration of organs in a slice, which may occur in separate data acquisition of SPECT and X-ray CT data. An external gamma ray source is needed to use gamma ray TCT. At present, there are five sources that are commercially available: ²⁴¹Am (59 keV, 432.2 y), ¹⁵³Gd (97, 103 keV, 241.6 d), ¹⁹⁵Au (99, 130 keV, 183.0 d), ⁵⁷Co (122, 137 keV, 271.8 d) and ¹³³Ba (356 keV, 10.52 y). Radionuclides having a long half-life can reduce the running cost of examinations. In the acquisition of TCT and ECT data, we have to separate two kinds of photons emitted from emission sources and transmission sources, and also eliminate scattered photons originating in both gamma ray sources from the measured counts. The scattered photons increase the measured events and result in decreasing the measured attenuation coefficients. This influence is not negligible when we use a parallel-hole collimator. Therefore, we have to devise some mechanism that eliminates gamma rays scattered in the body. Needless to say, we should convert the linear attenuation coefficient for the photo-peak energy of the external source to that of the emission source and correct the attenuation of gamma rays. As for the μ -map it is proven that statistical accuracy is not required so much in attenuation correction, so that we can measure TCT data in a relatively short time and use the reconstructed μ -map after spatial smoothing. On the other hand, when we use an X-ray CT image for the μ -map, an X-ray CT examina-

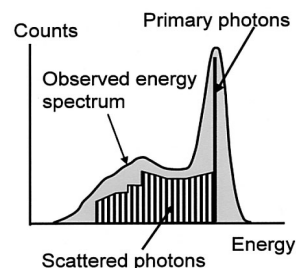


Fig. 8 Ideal energy spectrum and measured energy spectrum for ^{99m}Tc. The measured data are affected by the energy resolutions of a scintillator and PMTs.

tion is needed as an additional study. Then we have to convert the CT numbers to the gamma-ray linear attenuation coefficients of interest by a table look-up method. In any case, TCT is a troublesome task because an additional study using gamma ray TCT or X-ray CT is also needed. Nowadays, a compact all-in-one system that combines a SPECT system and an X-ray CT system is commercially available. In Japan, the handling of radionuclides as an external source is legally burdensome and expensive, ensuring that this system will become widely adopted because of its low running cost and ease of handling to obtain the μ -map.

4. SCATTERING OF GAMMA RAYS

4.1 Influence of scattered photons

Most gamma rays (primary photons or scattered photons) passing through collimator holes cause Compton scattering and/or photoelectric absorption in an NaI(Tl) scintillator. Compton scattering is a phenomenon in which a gamma ray collides with an orbital electron of an atom elastically, with the initial energy of the gamma ray divided between the electron and the scattered photon. The energy of a scattered photon is therefore always lower than its initial energy. On the other hand, when photoelectric absorption occurs, the incident gamma ray disappears and a photoelectron is generated. At this time, the atom with the excited state remains, and returns to the stable state by generating a fluorescent X-ray (wavelength: 410 nm) in the scintillator. In the case of Compton scattering, after scattering a few times, a photoelectron is generated by photoelectric absorption, and the same type of fluorescent X-ray is generated. The fluorescence plays an important role in the detection of gamma rays, but this fluorescence occurs non-uniformly in the scintillation crystal, so that the observed energy varies around the photo-peak energy. That is, a constant amount of fluorescence is not always observed by an incident gamma ray. When this fluorescence reaches the photocathode of a photo-multiplier tube (PMT), a photoelectron is discharged. This photoelectron is then accelerated by the high voltage applied to the PMT and collides with dynodes, with secondary electrons generated at these dy-

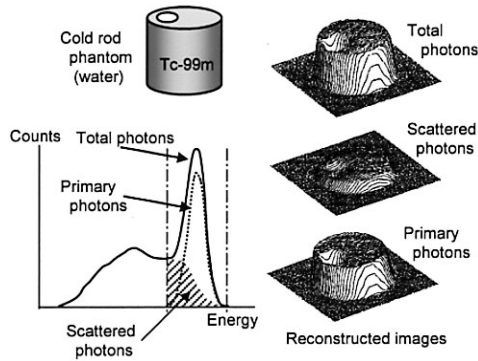


Fig. 9 Image distortion caused by scattered photons inside the object. In this simulation we assume a cold rod phantom with a 16 cm ϕ outer cylinder filled with ^{99m}Tc solution and a 3 cm ϕ inner cylinder filled with water. The projection data are calculated by the Monte Carlo method. Top right shows the image reconstructed with projections acquired by the conventional 20%-width energy window. Middle right shows the image reconstructed with projections which consist of scattered photons, and the bottom right shows that with projections which consist of primary photons.

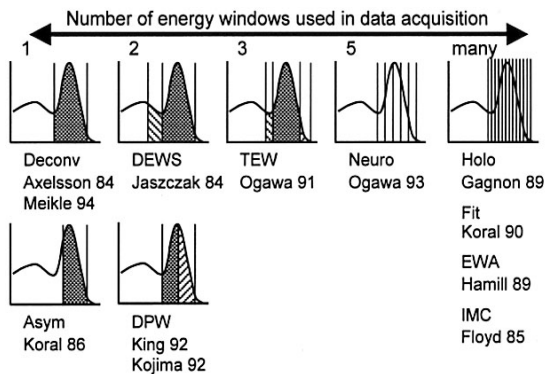


Fig. 10 Energy windows used for data acquisition and scatter correction.

nodes. As a result, a strong electric current is obtained in this amplification system. Because the number of photoelectrons that reach the photocathode varies locally and the number of secondary electrons generated at each dynode varies temporarily, statistical fluctuation occurs in the observed current. Ideally the spectrum of gamma rays should be monochrome (single energy), but the measured spectrum is broadened by the energy conversion of the above two steps (gamma ray to fluorescence and fluorescence to electric current). The broadened energy spectrum looks like the normal distribution and the energy resolution is reduced in the scintillation detector (Fig. 8). On the other hand, the electric charge generated by an incident gamma ray in the semiconductor detector is measured directly without any conversion of energy, so that the energy resolution becomes very high. In nuclear medicine, due to cost and performance considerations, the

NaI(Tl) scintillation detector with poor energy resolution is commonly used and thus many undesired scattered photons are detected just like primary photons with the conventional energy window with a width about twice the FWHM of the energy resolution. With this energy window we cannot separate scattered photons which have almost the same energy as the primary photons from the true primary photons, so that 40–50% of measured photons are scattered photons in ^{201}Tl imaging and 20–30% of measured photons are scattered photons in ^{99m}Tc imaging.^{87–90} For example, in myocardial SPECT with ^{201}Tl about a half of the measured counts are scattered photons and these photons do not provide any information on the location of the radionuclide from which the photons are emitted. These undesirable photons decrease the contrast resolution and spatial resolution in a reconstructed SPECT image, making the elimination of such scattered photons indispensable for quantitative SPECT imaging.

4.2 Scatter correction methods

Photons scattered in the human body are measured as if they are primary photons with the energy window set to the photo-peak. With these scattered photons the low frequency components of a reconstructed image increase and the contrast of this image decreases (Fig. 9). A feature of these scattered photons in a measured planar image is that the amount of the scattered photons varies pixel by pixel and the scatter fraction varies greatly according to the energy of a photon, the distribution of the scatterer, and the collimator used. Proposed methods for eliminating the scattered photons^{91–107} are categorized by the number of energy windows used for data acquisition (Fig. 10). In the deconvolution method (Deconv)⁹¹ a conventional energy window is used, and the scattered photons are removed from measured photons by a deconvolution process. The kernel used for the deconvolution is approximated to an exponential function, and this kernel is applied to the planar image or a reconstructed image. The point spread function (kernel) is a function of position, and this is influenced by the distribution of activity and attenuation coefficients. This method may therefore cause under- or over-correction. The asymmetric window method (Asym)⁹² is very simple, but it also eliminates primary photons at the same time. The methods that use two energy windows include the dual energy window subtraction method (DEWS)^{93,94} and dual photo-peak window method (DPW).^{95,128} In DEWS two planar images are acquired with the photo-peak energy window and the scatter window, and half of the counts measured by means of this scatter window are subtracted from the counts measured by the photo-peak window pixel by pixel. This method is simple and works well when the source is distributed uniformly in an object. In this method the photo-peak window measures the primary photon and the scattered photons including mainly the first- and second-order scattered photons. On the other hand, the scatter

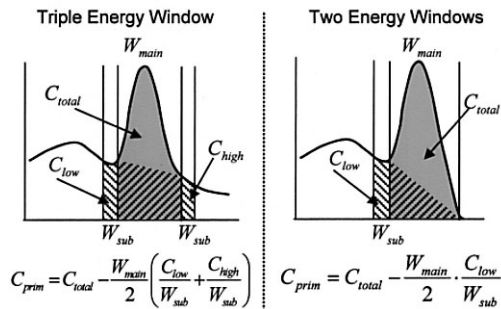


Fig. 11 Two types of energy window settings in the TEW method. In the dual-isotope SPECT study or SPECT study by means of a radioisotope having two or more photo-peaks in the energy spectrum, we set three energy windows and estimate scattered photons with a trapezoidal rule. If the targeted radioisotope has a single photo-peak, we neglect the right-hand sub-window and set two energy windows to the photo-peak.

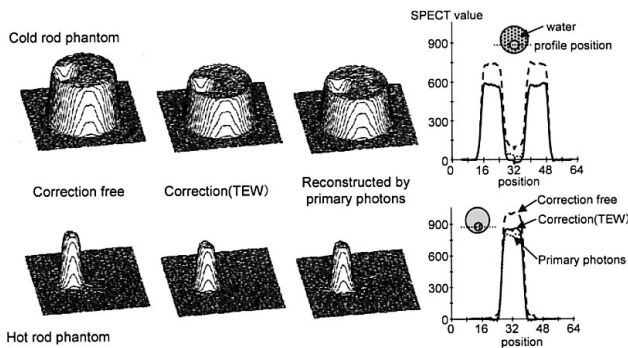


Fig. 12 Scatter correction with the TEW method for two types of activity distributions: a cold rod phantom and hot rod phantom. From left to right, images without scatter correction, those corrected by the TEW method and those reconstructed with projections which consist of primary photons, and profiles of these images.

window measures the higher order Compton scattered photons. The distribution of lower order scattered photons differs from that of the higher order scattered photons, so that the performance of this method is not always adequate. The DPW method measures photons with two energy windows dividing a photo-peak into two parts symmetrically and estimates the counts of scattered photons by a regression method.⁹⁵ This method is sensitive to photo-peak energy, but the high voltage of PMTs sometimes varies slightly, mandating that this method be carefully implemented in clinical situations. The triple energy window (TEW) method^{96–98} uses three energy windows (one main window and two sub-windows) set around the photo-peak (see Fig. 11) and estimates scattered photons measured by the main window pixel by pixel with the counts measured by two sub-windows. In order to improve the correction accuracy, one may slightly change the width and location of these sub-windows. The

removal of the scattered photons results in decreasing the measured events, so that distortion due to statistical noise may occur on an image. Hence it is desirable to apply an appropriate low-pass filter to the scatter-eliminated measured data (planar images). Though the TEW method is very simple, it is an efficient and stable method in clinical situations. The method which is based on an artificial neural network (Neuro)⁹⁹ uses five energy windows set around the photo-peak. With the training data generated by a Monte Carlo simulation, the artificial neural network estimates the amount of primary photons in measured data. The performance of estimation in this method is superior to that of the TEW method, because it accounts for energy spectra roughly measured by five energy windows. Moreover, this method withstands statistical noise because the energy window is relatively wide and it estimates the counts of primary photons in a manner just like pattern recognition. On the other hand, there are some methods that use more than five narrow energy windows. The holospectral method (Holo)¹⁰⁰ measures an energy spectrum at each pixel position with narrow windows with a width of 2 keV, and estimates the counts of primary photons by means of the principal component analysis method. The counts measured with the narrow energy window are strongly influenced by statistical noise, so this method is not effective except in the case of adequate counts. The energy weighted acquisition (EWA) method¹⁰¹ compensates for scattered photons by adding the counts of acquired photons multiplied by a weighing factor determined in advance. Actually this weighing factor varies according to the activity distribution and μ -map, so that this method may not yield quantitative results. The spectrum fitting (Fit) method¹⁰² estimates an energy spectrum of primary photons with the idea that the energy spectrum of the primary photons can be approximated by the normal distribution. In this method the statistical noise that is introduced in projection data measured with narrow energy windows degrades the accuracy of estimation. The inverse Monte Carlo (IMC) method¹⁰³ calculates an original source location from the energy of an observed photon and its position with the help of the Monte Carlo simulation. This method requires a heavy computational load and is not applicable to clinical study. The other scatter correction methods include the transmission dependent scatter correction (TDSC) method^{104,105} and the iterative correction method which eliminates scattered photons in the image reconstruction with MAP-EM or OS-EM.^{106,107} The TDSC method iteratively estimates the distribution of scattered photons with the help of the μ -map. This method is well established but requires more information on the μ -map. A statistical approach such as the ML-EM method requires a model for distribution of scattered photons and takes a long time to correct scattered photons when a three dimensional kernel is used. And this model should be well designed with the help of experiments and simulations.

With the above observations we can see that the accurate estimation of scattered photons requires knowledge of the accurate shape of the energy spectrum, but too narrow an energy window introduces statistical noise into acquired data. So a compromise is needed between spectral accuracy and statistical noise. If we review these methods from the standpoint of the scatter fraction which varies pixel by pixel depending on the distribution of source and attenuation coefficients, most of the methods proposed in the 1980s did not consider variation in this scatter fraction, so that a marked correction effect was not obtained with these correction methods. On the other hand, the methods proposed in the 1990s consider this point so that sufficient scatter correction was established. Among these methods the TEW method yields good performance (Fig. 12). This method is applicable to SPECT study with a radionuclide having more than two photo-peaks or with two radionuclides with different photo-peak energies.¹¹⁰ Moreover, we can increase the accuracy of estimation of primary photons by means of only two energy windows if the radionuclide has a single photo-peak such as ^{99m}Tc (see Fig. 11). So this method or a modified version of this method is implemented in most of the commercially available SPECT systems due to its performance accuracy, speed and ease of implementation.

As a related topic, there is a problem in the characteristic X-rays generated by the photoelectric absorption in the lead collimator.^{108,109} These characteristic X-ray photons (72, 74, 84, and 87 keV (L-shell – K-shell)) are observed in the conventional energy window for the measurement of primary photons (²⁰¹Tl) and become a subject of discussion in ^{99m}Tc-²⁰¹Tl or ¹²³I-²⁰¹Tl dual-radionuclide studies. The elimination of scattered photons in the dual-isotope imaging with ^{99m}Tc-¹²³I is also important and a few methods have been proposed.^{110–113,129} The removal of these scattered photons is also indispensable in quantitative SPECT imaging.

5. COLLIMATOR APERTURE

5.1 Role of a collimator

A collimator is indispensable to specify the flight direction of gamma rays from a single photon emission radionuclide.^{114,115} The collimator has been used since H.O. Anger developed the first gamma camera system in the 1950s. The size of a collimator hole relates to the sensitivity and spatial resolution of a gamma camera, so that the collimator is very important in determining the quality of scintigrams and SPECT images. The collimator commonly used in nuclear medicine is a parallel-hole type, which is composed of numerous parallel-holes aligned orthogonally to the collimator surface. The typical dimensions of a collimator hole used for detecting low-energy gamma rays are hole width 1–2 mm, hole height 30–40 mm and septum width 0.1–0.2 mm. The material of the

collimator is lead or tungsten which has high performance in shielding against photons that enter a collimator from an undesirable direction. The shape of the hole depends on the manufacturing method, and there are hexagonal, round and square holes. The thickness of the septum between holes is designed to control the number of photons penetrating through the septum. This penetration ratio is defined by $\exp(-\mu w)$, where μ is the linear attenuation coefficient and w is the total path-length of a gamma ray in the septum. μ is inherent in each material and is a function of energy. The ratio $\exp(-\mu w)$ is usually designed at 0.02–0.05. The reasons why lead is commonly used as the material for a collimator are as follows: high shielding efficiency (large atomic number), low cost and ease of manufacturing. The spatial resolution and the sensitivity of a gamma camera are closely related to the size and the number of holes in the collimator. The smaller the hole, the higher is the spatial resolution. The spatial resolution of a planar image is decided not only by the specifications of the collimator but also relates to the positional detection mechanism of the scintillator and PMTs. This resolution is called intrinsic resolution and this is a particular value depending on the detection systems including the scintillator and PMTs. On the other hand, the spatial resolution of a parallel-hole collimator is a function of the distance between the source and the collimator surface. When this distance is great, the spatial resolution becomes worse. The spatial resolution of the system is about 10–15 mm in FWHM at a distance of 15 cm from the collimator surface.

The sensitivity of a gamma camera is not only affected by the design of the collimator but also the scintillator. The sensitivity of the scintillator depends on its thickness, i.e., if this thickness is long, many photons may interact with atoms composing the scintillator by the photoelectric absorption. This sensitivity is generally very high. On the other hand, the sensitivity of a collimator, which means how many photons pass through the collimator, is very low. For example, the sensitivity of a low-energy parallel-hole collimator is about 100 cps (count/sec) for a point source (^{99m}Tc) with 1 MBq in the air 10 cm from the surface of the collimator. The width of the energy window is 20%. This means that only $100/1000000 = 0.01\%$ will be observed by a gamma camera and about 99.99% will be discarded. This is a serious problem and in order to improve efficiency, electrical collimation systems have been studied by some researchers. The most popular candidate is a Compton camera with which photons are detected by two detectors without any mechanical collimators. This method is now being thoroughly investigated as a next generation gamma camera.

The basic structure of the collimator is a hole with a finite length and aperture size. Thus, the photons which pass through an individual hole are not only photons entering a hole parallel to the hole axis but also photons entering the hole at a small angle to the hole axis. As a

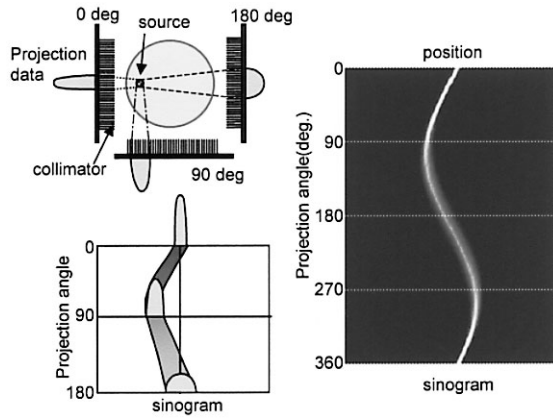


Fig. 13 A point source and an obtained sinogram. Projection data differ from each other depending on the geometry of the point source and location of the collimator. The sinogram also varies with the measured angle.

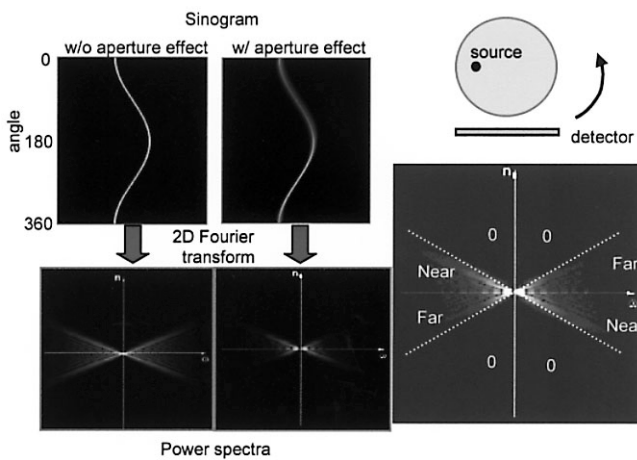


Fig. 14 An ideal sinogram and a sinogram affected by the collimator aperture (*left top*). The Fourier transforms of these two sinograms are shown below them. The power spectrum of the ideal projection data shows a bow tie shape. On the other hand, the collimator aperture decreases the high frequency component of the sinogram. The correction of the collimator aperture effect is performed by applying a kind of high emphasis filter in the Fourier domain. The right image shows the corrected power spectrum.

result, each hole accepts all of the photons in a cone at a small vertex angle. This is the reason why the spatial resolution of a collimator is a function of the distance between a source and the collimator surface. This introduces a blurring in a SPECT image. The point-spread function of the collimator has a shift-variant property and it is very difficult to eliminate this blurring.

5.2 Influence of the collimator aperture

The detected gamma rays are generally supposed to be emitted from a source located in a strip area (rectangular area with a certain constant width). To measure such ideal

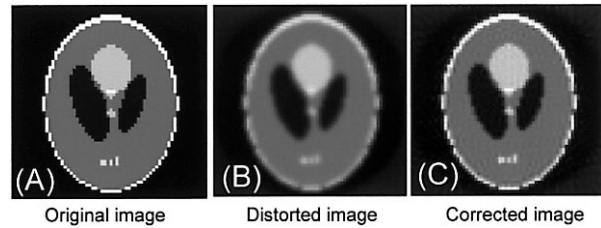


Fig. 15 Correction of the collimator aperture effect with the FDR concept. From left to right, (A) an original image (Shepp phantom), (B) an image distorted by the collimator aperture and (C) one corrected with the FDR concept. The aperture angle is 2 degrees.

projection data the length of a hole should be infinite and the aperture should be of infinitely small size. But in actual conditions, a hole has a finite length (e.g. 3–4 cm), and the size of its aperture is likewise finite (e.g. 1–2 mm in diameter). Thus the photons located in a cone area may be detected with the detector. As a result, the shape of the point-spread function varies according to the distance between the source and the collimator surface. That is, if this distance is short, the shape of the PSF is close to the ideal one (rectangular function), while if it is long, the shape approaches that of the normal distribution. On the other hand, the sensitivity of the collimator does not depend on the distance between the source and the collimator; i.e., the constant. The amplitude of the PSF therefore becomes low when the distance increases. If we reconstruct a SPECT image with the projection data being affected by the aperture effect, blurring occurs in the reconstructed image, because data acquired in a conic area are backprojected into a strip area on an image plane. Moreover, since the PSF is a function of the distance between the source position and the surface of the collimator, the blurring function on a reconstructed image varies with the radius, and the blurring function becomes concentric circles. The blurring at the center is isotropic whereas that in areas far from the center of an image plane is not isotropic. The influence of this blurring results in distortion in a reconstructed image. Figure 13 illustrates the projection data for 0, 90 and 180 degrees that are obtained from the phantom in which a source is located to the left of the center. If there is no aperture effect on the projection data, this sinogram should be a sine curve with a constant width. In fact, the projection data are influenced by the aperture effect, so that the sinogram varies in its width and density depending on the projection angle.

5.3 Correction methods for the collimator aperture

As for correction of the distortion caused by a collimator aperture, a filtering operation was used in the 1980s.¹¹⁶ This method was a kind of shift-invariant processing. But the shift variant operation used in the Fourier domain was proposed in the late 1980s,^{117,118} and these correction methods have been studied. Xia et al. proposed the most

popular method, which is based on the concept of “frequency distance relation” (FDR).¹¹⁹ Figure 14 shows a sinogram of a point source up to 360 degrees. The left one shows the ideal projection data without the aperture effect, and the right one the data reflecting the aperture effect. When the influence of the aperture occurs, a large burring is caused in the direction of the angle where the distance of the source and the detector is large. At the same time the density value decreases in that view angle. The power spectra after Fourier transform in the horizontal axis (position of the detector) and in the vertical axis (view angle) are shown under these sinograms. Both power spectra look like bow ties. In the ideal case the bow tie has a left-right symmetry, but in the case influenced by the aperture the bow tie is asymmetrical. The bright part corresponding to the large value shrinks near the diagonal. This means that the high frequency component in this direction has small values. This part corresponds to the angular region where the large burring is generated on the sinogram space. Therefore, to expand the shape of the bow tie in the directions of small values means to recover the high frequency component in these directions and make it close to the ideal projection data. To accomplish this we operate a kind of high emphasis filter in the Fourier domain. After the filtering we take an inverse Fourier transform into the filtered data and obtain projection data which are corrected by the aperture effect. The correction method in the Fourier space basically increases the high frequency components. Therefore, one should take note of noise which is inevitably introduced. Figure 15 shows the image corrected by means of the FDR concept. Other approaches with a statistical reconstruction method such as ML-EM or OS-EM^{120–122} and iterative correction methods^{123,124} have also been proposed and the corrected images have good accuracy. In the case of these iterative approaches, an appropriate model and long calculation time, especially with three-dimensional correction, are required.

6. SUMMARY

This paper reviewed some of the problems associated with quantitative SPECT imaging and a number of correction methods developed by many researchers. The distortions in the SPECT image relate to several factors mentioned above, mandating that physicians and technologists who acquire projection data and reconstruct images be well aware of them. Correct understanding and management help to ensure the usefulness of SPECT as a tool for measuring various organ functions in the clinical setting.

ACKNOWLEDGMENTS

The author thanks Mr. Akira Ishikawa (Graduate School of Hosei University) for his assistance in performing some simulation studies. This work was supported in part by the Ministry

of Education, Culture, Sports, Science and Technology, Grant-in-Aid for Scientific Research (B) 16390344.

REFERENCES

1. Webb S, ed. *The Physics of Medical Imaging*, Adam Hilger, 1988: 142–318.
2. Barrett HH, Swindell W. *Radiological Imaging (Vol. 1)*, Academic Press, 1981: 259–290.
3. Ell PJ, Holman BL, eds. *Computed Emission Tomography*, Oxford University Press, 1982.
4. Sorenson JA, Phelps ME, eds. *Physics in Nuclear Medicine (2nd edition)*, W.B. Saunders Company, 1987: 298–464.
5. Herman GT, ed. *Topics in Applied Physics. Image Reconstruction from Projections*, Springer-Verlag, 1979: 147–246.
6. Brooks RA, Dichiuro G. Principles of computed assisted tomography (CAT) in radiographic and radioisotopic imaging. *Phys Med Biol* 1976; 5: 689–732.
7. Jaszczak RJ, Coleman RE. Single photon emission computed tomography (SPECT): principles and instrumentation. *Invest Radiol* 1985; 20: 897–910.
8. Larsson SA. Gamma camera emission tomography: development and properties of a multi-sectional emission computed tomography system. *Acta Radiol Suppl* 1980; 363: 1–75.
9. Sorenson JA. Method for quantitative measurement of radioactivity *in vivo* by whole-body counting. In *Instrumentation in nuclear medicine, Vol. 2*. Hine GJ, Sorenson JA (eds.), New York; Academic Press, 1974: 311–348.
10. Zaidi H. Quantitative SPECT: Recent developments in detector response, attenuation and scatter compensation techniques. *Physica Medica* 1996; XII: 101–117.
11. Parker JA. Quantitative SPECT: basic theoretical considerations. *Semin Nucl Med* 1989; 19: 3–12.
12. Murphy PH. Quantitative emission tomography. *J Nucl Med* 1987; 5: 922–923.
13. Jaszczak RJ, Coleman RE, Whitehead FR. Physical factors affecting quantitative measurements using camera-based single photon emission computed tomography (SPECT). *IEEE Trans Nucl Sci* 1981; 28: 69–80.
14. Blockland KAK, Reiber HC, Pauwels EKJ. Quantitative analysis in single photon emission tomography (SPET). *Eur J Nucl Med* 1992; 19: 47–61.
15. Eisner RL, Nowak DJ, Pettigrew R, Fajman W, LaCroix KJ, Tsui BMW, et al. A comparison of 180 degrees and 360 degrees acquisition for attenuation-compensated thallium-201 SPECT images. *J Nucl Med* 1998; 39: 562–574.
16. Go RT, MacIntyre WJ, Houser TS, Pantoja M, Odonnell JK, Feiglin DH, et al. Clinical evaluation of 360 degrees and 180 degrees data sampling techniques for transaxial SPECT thallium-201 myocardial perfusion imaging. *J Nucl Med* 1985; 26: 695–706.
17. Knesaurek K, King MA, Glick SJ, Penney BC. Investigation of causes of geometric distortion in 180 degrees and 360 degrees angular sampling in SPECT. *J Nucl Med* 1989; 30: 1666–1675.
18. Tamaki N, Mukai T, Ishii Y, Fujita T, Yamamoto K, Minato K, et al. Comparative study of thallium emission myocardial tomography with 180 degrees and 360 degrees data collection. *J Nucl Med* 1982; 23: 661–666.
19. Nuyts J, Dupont P, Van den Maegdenbergh V, Vleugels S,

- Suetens P, Mortelmans L. A study of heart-liver artifacts in emission tomography. *J Nucl Med* 1995; 36: 133–139.
20. LaCroix KJ, Tsui BMW, Hasegawa BH. A comparison of 180 degrees and 360 degrees acquisition for attenuation-compensated thallium-201 SPECT images. *J Nucl Med* 1998; 39: 562–574.
 21. Shepp LA, Vardi Y. Maximum likelihood reconstruction for emission tomography. *IEEE Trans Med Imag* 1982; 1: 113–122.
 22. Lange K, Carson R. EM reconstruction algorithm for emission and transmission tomography. *J Compt Assist Tomogr* 1984; 8: 306–316.
 23. Vardi Y, Shepp LA, Kaufman L. A statistical model for positron emission tomography. *J Amer Statist Assoc* 1985; 80: 8–37.
 24. Lange K, Bahn M, Little R. A theoretical study of some maximum likelihood algorithms for emission and transmission tomography. *IEEE Trans Med Imag* 1987; 6: 106–114.
 25. Geman S, Geman D. Stochastic relaxation, Gibbs distributions and the Bayesian reconstruction of images. *IEEE Trans Pattern and Machine Intell* 1984; 6: 721–741.
 26. Geman S, McClure D. Bayesian image analysis: An application to single photon emission tomography. *Proc Amer Statist Assoc Stat Comp* 1985; Sect: 12–18.
 27. Levitan E, Herman GT. A maximum a posteriori probability expectation maximization algorithm for image reconstruction in emission tomography. *IEEE Trans Med Imag* 1987; 6: 185–192.
 28. Lalush DS, Tsui BMW. Simulation evaluation of Gibbs prior distributions for use in maximum a posteriori SPECT reconstructions. *IEEE Trans Med Imag* 1992; 11: 267–275.
 29. Hudson HM, Larkin R. Accelerated image reconstruction using ordered subsets of projection data. *IEEE Trans Med Imag* 1994; 13: 601–609.
 30. Byrne CL. Block-iterative methods for image reconstruction from projections. *IEEE Trans Imag Proc* 1996; 5: 792–794.
 31. Byrne CL. Accelerating the EMLL algorithm and rescaled iterative algorithms by rescaled block-iterative method. *IEEE Trans Imag Proc* 1998; 7: 100–109.
 32. Takahashi M, Ogawa K. Selection of projection set and the ordered of calculation in ordered subsets expectation maximization method. In *IEEE Nucl Sci Symp and Med Imag Conf Rec, vol. 2, 1997*: 1408–1412.
 33. Takahashi Y, Murase K, Mochizuki T, Higashino H, Sugawara Y, Kinda A. Evaluation of the number of SPECT projections in the ordered subsets-expectation maximization image reconstruction method. *Ann Nucl Med* 2003; 17: 525–530.
 34. Tsui BMW, Segars WP, Lalush DS. Effects of Upward Creep and Respiratory Motions in Myocardial SPECT. *IEEE Trans Nucl Sci* 2000; 47: 1192–1195.
 35. Kay DB, Keyes Jr JW. First order correction for absorption and resolution compensation in radionuclide Fourier tomography. *J Nucl Med* 1975; 16: 540–541.
 36. Budinger TF. Quantitative nuclear medicine imaging, application of computers to the gamma camera and whole body scanner. In *Recent Advances in Nuclear Medicine*, Lawrence JH, ed. Vol. IV, New York; Grune & Stratton, 1974: 41–130.
 37. Budinger TF, Gullberg GT. Transverse section reconstruction of gamma-ray emitting radionuclides in patients. In *Reconstruction tomography in diagnostic radiology and nuclear medicine*. Ter-Pergossian MM, Phelps ME, Brownell GL, Cox Jr JR, Davis DO, Evans RG, eds. Baltimore; University Park Press, 1977: 315–342.
 38. Budinger TF, Gullberg GT, Huesman RH. Emission computed tomography. In *Image Reconstruction from Projections*. Herman GT, ed. vol. 32, New York; Springer-Verlag, 1979: 147–246.
 39. Chang LT. A method for attenuation correction in radionuclide computed tomography. *IEEE Trans Nucl Sci* 1978; 25: 638–643.
 40. Chang LT. Attenuation correction and incomplete projection in single photon emission computed tomography. *IEEE Trans Nucl Sci* 1979; 26: 2780–2789.
 41. Morozumi T, Nakajima M, Ogawa K, Yuta S. Attenuation correction method for single photon emission CT. *Trans IEICE* 1983; J-66-D 10: 1130–1136.
 42. Morozumi T, Nakajima M, Ogawa K, Yuta S. Attenuation correction method using the ratio of two projections calculated without and with the attenuation for SPECT. *Trans IEICE* 1984; J-67-D 7: 800–806.
 43. Bellini S, Piacentini M, Cafforio C, Rocca F. Compensation of tissue absorption in emission tomography. *IEEE Trans Acoust Speech Signal Process* 1979; 27: 213–218.
 44. Tretiak OJ, Metz CE. The exponential Radon transform. *SIAMJ Appl Math* 1980; 39: 341–354.
 45. Tanaka E. Quantitative image reconstruction with weighted backprojection for single photon emission tomography. *J Compt Assist Tomogr* 1983; 7: 692–700.
 46. Natterer F. *The mathematics of computerized tomography*. New York; Wiley, 1986.
 47. Inouye T, Kose K, Hasegawa A. Image reconstruction algorithm for single photon emission computed tomography. *Phys Med Biol* 1989; 39: 299–304.
 48. Metz CE, Pan X. A unified analysis of exact methods of inverting the 2D exponential Radon transform with implications for noise control in SPECT. *IEEE Trans Med Imag* 1995; 14: 643–658.
 49. Liang Z. Compensation for attenuation, scatter and detector response in SPECT reconstruction via iterative FBP methods. *Med Phys* 1993; 20: 1097–1106.
 50. Budinger TF, Gullberg GT. Three-dimensional reconstruction in nuclear medicine emission imaging. *IEEE Trans Nucl Sci* 1974; 21: 2–20.
 51. Gustafson DE, Berggren MJ, Singh M, Dewanjee MK. Computed transaxial imaging using single gamma emitters. *Radiology* 1978; 129: 187–194.
 52. Walters TE, Simon W, Chesler DA, Correia JA. Attenuation correction in gamma emission computed tomography. *J Compt Assist Tomogr* 1981; 5: 89–94.
 53. Soussaline FP, Cao A, Le Coq G, Raynaud C, Kellershohn C. An analytical approach to single photon emission computed tomography with the attenuation effect. *Eur J Nucl Med* 1982; 7: 487–493.
 54. Axelsson B, Israelsson AL, Larsson SA. Studies of a technique for attenuation correction in single photon emission computed tomography. *Phys Med Biol* 1987; 32: 737–749.
 55. Tsui BMW, Zhao XD, Frey EL, Gullberg GT. Comparison between ML-EM and WLS-CG algorithms for SPECT image reconstruction. *IEEE Trans Nucl Sci* 1991; 38: 1766–

- 1772.
56. Tsui BMW, Terry JA, Gullberg GT. Evaluation of cardiac cone-beam single photon emission computed tomography using performance experiments and receiver operating characteristic analysis. *Invest Radiol* 1993; 28: 1101–1112.
 57. Ogawa K, Takagi Y, Kubo A, Hashimoto S, Sanmiya T, Okano Y, et al. An attenuation correction method for single photon emission computed tomography using gamma ray transmission CT. *KAKU IGAKU (Jpn J Nucl Med)* 1985; 22: 477–490.
 58. Natterer F. Inversion of the attenuated Radon transform. *Inverse Problem* 2001; 17: 113–119.
 59. Kunyansky LA. A new SPECT reconstruction algorithm based on the Novikov's explicit inversion formula. *Inverse Problem* 2001; 17: 293–306.
 60. Guillement JP, Jauberteau F, Kunyansky L, Novikov R, Trebossen R. On single-photon emission computed tomography imaging based on an exact formula for the nonuniform attenuation correction. *Inverse Problems* 2002; 18: L11–L19.
 61. Wen J, Li T, Liang Z. An analytical inversion of the nonuniformly attenuated Radon transform with variable focal-length fan-beam collimators. *IEEE Trans Nucl Sci* 2003; 50: 1641–1649.
 62. Manglos SH, Young TM. Determination of the attenuation map from SPECT projection data alone. *J Nucl Med* 1993; 35: 193.
 63. Moore SC, Kijewski MF, Mueller SP. A general approach to non-uniform attenuation correction using emission data alone. *J Nucl Med* 1997; 38: 246.
 64. Gullberg GT, Malko JA, Eisner RL. Boundary definition. In *Emission computed tomography—Current trends*. New York: The Society of Nuclear Medicine, 1983: 33–53.
 65. Hosoba M, Wani H, Toyama H, Murata H, Tanaka E. Automated body contour detection in SPECT: effects on quantitative studies. *J Nucl Med* 1989; 27: 1184–1191.
 66. Ben Younes R, Mas J, Bidet R. Fully automated detection algorithm: the preliminary step for scatter and attenuation compensation in SPECT. *Eur J Nucl Med* 1988; 14: 586–589.
 67. Macey DJ, DeNardo GL, DeNardo SJ. Comparison of three boundary detection methods for SPECT using Compton scattered photons. *J Nucl Med* 1988; 29: 203–207.
 68. Herbert TJ, Gopal SS, Murphy P. Fully automated optimization algorithm for determining the 3-D patient contour from photo-peak projection data in SPECT. *IEEE Trans Med Imag* 1995; 14: 122–131.
 69. Manglos SH, Jaszczak RJ, Floyd CE, Hahn LJ, Greer KL, Coleman RE. Nonisotropic attenuation in SPECT: phantom tests of quantitative effects and compensation techniques. *J Nucl Med* 1987; 28: 1584–1591.
 70. Ogawa K, Kubo A, Hashimoto S, Morozumi T, Nakajima M, Yuta S, et al. An attenuation correction of SPECT image transmission data acquired with dual head gamma camera system. *Med Imag Tech* 1985; 3s: 103–104.
 71. Malko JA, Van Herten RL, Gullberg GT, Kowalsky WP. SPECT liver imaging using an iterative attenuation algorithm and an external flood source. *J Nucl Med* 1986; 27: 701–705.
 72. Bailey DL, Hutton BF, Walker PJ. Improved SPECT using simultaneous emission and transmission Tomography. *J Nucl Med* 1987; 28: 844–851.
 73. Tsui BMW, Gullberg GT, Edgerton ER, Ballard JG, Perry JR, McCartney WH, et al. Correction of non-uniform attenuation in cardiac SPECT imaging. *J Nucl Med* 1989; 30: 497–507.
 74. Ljungberg M. Development and evaluation of attenuation and scatter correction techniques for SPECT using the Monte Carlo method. PhD Thesis, Lund University, Sweden, 1990.
 75. Manglos SH, Bassano DA, Duxbury CE, Capone RB. Attenuation maps for SPECT determined using cone beam transmission computed tomography. *IEEE Trans Nucl Sci* 1990; 37: 600–608.
 76. Manglos SH, Bassano DA, Thomas FD, Grossman ZD. Imaging of human torso using cone beam transmission CT implemented on a rotating gamma camera. *J Nucl Med* 1992; 33: 150.
 77. Cao ZJ, Tsui BMW. Performance characteristics of transmission imaging using a uniform sheet source with parallel hole collimation. *Med Phys* 1992; 19: 1205–1212.
 78. Celler A, Sitek A, Stoub E, Hawman P, Harrop R, Lyster D. Multiple line source array for SPECT transmission scans: simulation, phantom and patient studies. *J Nucl Med* 1998; 39: 2183–2189.
 79. Almquist H, Palmer J, Ljungberg M, Wollmer P, Jonson B, Strand S-E. Quantitative SPECT by correction of the projection set using transmission data: evaluation of a method. *Eur J Nucl Med* 1990; 16: 587–594.
 80. Greer KL, Harris CC, Jaszczak RJ, Coleman RE, Hedlund LW, Floyd CE, et al. Transmission computed tomography data acquisition with a SPECT system. *J Nucl Med Tech* 1987; 15: 53–56.
 81. Tung C-H, Gullberg GT, Zeng GL, Christian PE, Datz FL, Morgan HT. Non-uniform attenuation correction using simultaneous transmission and emission converging tomography. *IEEE Trans Nucl Sci* 1992; 39: 1134–1143.
 82. Kalki K, Blankespoor SC, Brown JK, Hasegawa BH, Dae MW, Stillson C. Myocardial perfusion imaging with a combined X-ray CT and SPECT system. *J Nucl Med* 1978; 38: 1530–1540.
 83. Fleming JS. A technique for using CT images in attenuation correction and quantification in SPECT. *Nucl Med Commun* 1989; 10: 83–97.
 84. Rowell NP, Glaholm J, Flower MA, McCreedy VR. Anatomically derived attenuation coefficients for use in quantitative single photon emission tomography studies of the thorax. *Eur J Nucl Med* 1992; 19: 36–40.
 85. Takahashi Y, Murase K, Higashino H, Mochizuki T, Motomura N. Attenuation correction of myocardial SPECT images with X-ray CT: Effect of registration errors between X-ray CT and SPECT. *Ann Nucl Med* 2002; 16: 431–435.
 86. Kashiwagi T, Yutani K, Fukuchi M, Naruse H, Iwasaki T, Yokozuka K, et al. Correction of nonuniform attenuation and image fusion in SPECT imaging by means of separate X-ray CT. *Ann Nucl Med* 2002; 16: 255–261.
 87. Floyd CE, Jaszczak RJ, Harris CC, Coleman RE. Energy and spatial distribution of multiple order Compton scatter in SPECT: A Monte Carlo simulation. *Phys Med Biol* 1984; 29: 1217–1230.
 88. Floyd CE, Jaszczak RJ, Coleman RE. Scatter detection in SPECT imaging: dependence on source depth, energy, and

- energy window. *Phys Med Biol* 1988; 33: 1075–1081.
89. Ogawa K, Harata Y, Ichihara T, Kubo A, Hashimoto S. Estimation of scatter components in SPECT planar image using a Monte Carlo method. *KAKU IGAKU (Jpn J Nucl Med)* 1990; 27: 467–476.
 90. Maeda S, Ogawa K. Quantitative assessment of scattered photons considering skull bone in brain SPECT. *KAKU IGAKU (Jpn J Nucl Med)* 1994; 31: 431–439.
 91. Axelsson B, Msaki B, Israelsson A. Subtraction of Compton-scattered photons in single-photon emission computerized tomography. *J Nucl Med* 1984; 25: 490–494.
 92. Koral KF, Swailem FM, Buchbinder S, Clinthone NH, Rogers WL, Tsui BMW. SPECT dual-energy-window Compton correction: scatter multiplier required for quantification. *J Nucl Med* 1990; 31: 90–98.
 93. Jaszczak RJ, Greer KL, Floyd CE, Harris CC, Coleman RE. Improved SPECT quantification using compensation for scattered photons. *J Nucl Med* 1984; 25: 893–900.
 94. Lowry CA, Cooper MJ. The problem of Compton scattering in emission tomography: a measurement of its spatial distribution. *Phys Med Biol* 1987; 32: 1187–1191.
 95. King MA, Hademenos GJ, Glick SJ. A dual-photopeak window method for scatter correction. *J Nucl Med* 1992; 33: 605–612.
 96. Ogawa K, Harata Y, Ichihara T, Kubo A, Hashimoto S. A practical method for position-dependent Compton-scatter correction in single photon emission CT. *IEEE Trans Med Imag* 1991; 10: 408–412.
 97. Ogawa K, Ichihara T, Kubo A. Accurate scatter correction in single photon emission CT. *Ann Nucl Med Sci* 1994; 7: 145–150.
 98. Ichihara T, Ogawa K, Motomura N, Hasegawa H, Hashimoto J, Kubo A. Compton-scatter compensation using the triple energy window method for single and dual isotope SPECT. *J Nucl Med* 1993; 34: 2216–2221.
 99. Ogawa K, Nishizaki N. Accurate scatter compensation using neural networks in radionuclide imaging. *IEEE Trans Nucl Sci* 1993; 40: 1020–1024.
 100. Gagnon D, Todd-Pokropek AE, Arsenault A, Dupras G. Introduction to holospectral imaging in nuclear medicine for scatter subtraction. *IEEE Trans Med Imag* 1989; 8: 245–250.
 101. Hamill JJ, DeVito RP. Scatter reduction with energy-weighted acquisition. *IEEE Trans Nucl Sci* 1989; 36: 1334–1339.
 102. Koral KF, Wang X, Rogers WL, Clinthone NH, Wang X. SPECT Compton-scattering correction by analysis of energy spectra. *J Nucl Med* 1988; 29: 195–202.
 103. Floyd CE, Jaszczak RJ, Greer KL, Coleman RE. Inverse Monte Carlo as a unified reconstruction algorithm for ECT. *J Nucl Med* 1986; 27: 1577–1585.
 104. Meikle SR, Hutton BF, Bailey DL. A transmission dependent method for scatter correction in SPECT. *J Nucl Med* 1994; 35: 360–367.
 105. Narita Y, Eberl S, Iida H, Hutton BF, Braun M, Nakamura T, et al. Monte Carlo and experimental evaluation of accuracy and noise properties of two scatter correction methods for SPECT. *Phys Med Biol* 1996; 41: 2481–2496.
 106. Kadrmas DJ, Frey EC, Karimi SS, Tsui BMW. Fast implementations of reconstruction-based scatter compensation in fully 3D SPECT image reconstruction. *Phys Med Biol* 1998; 43: 857–874.
 107. Tsui BMW, Frey EC, LaCroix KJ, Lalush DS, McCartney WH, King MA, et al. Quantitative Myocardial Perfusion SPECT. *J Nucl Cardiol* 1998; 5: 507–522.
 108. Motomura N, Ichihara T, Hasegawa H, Ogawa K, Hashimoto J, Kubo A. Development of a lead x-ray compensation method in simultaneous Tl-201 SPECT & Tc-99m TCT using a flood source. *IEEE Trans Nucl Sci* 1997; 44: 2459–2464.
 109. Wang WT, Frey EC, Tsui BMW, Tocharoenchai C, Baird WH. Parameterization of Pb X-ray contamination in simultaneous Tl-201 and Tc-99m dual-isotope imaging. *IEEE Trans Nucl Sci* 2002; 49: 680–692.
 110. Ogawa K. Simulation study of triple-energy-window scatter correction in combined Tl-201, Tc-99m SPECT. *Ann Nucl Med* 1994; 8: 277–281.
 111. Matsunaga A, Ogawa K. Scatter correction in multi-radioclide data acquisition by means of a neural network. In *IEEE Conf Rec of Med Imag Conf, vol. 2*, 1999: 948–952.
 112. El Fakhri G, Maksud P, Habert MO, Todd-Pokropek A, Aurengo A. A new correction method for cross-talk using artificial neural network: validation in simultaneous technetium and iodine cerebral imaging. In *IEEE Conf Rec of Med Imag Conf, vol. 2*, 1999: 1000–1004.
 113. El Fakhri G, Moore SC, Maksud P, Aurengo A, Kijewski MF. Absolute activity quantitation in simultaneous ¹²³I/^{99m}Tc brain SPECT. *J Nucl Med* 2001; 42: 300–308.
 114. Moore SC, Kouris K, Cullum I. Collimator design for single photon emission tomography. *Eur J Nucl Med* 1992; 19: 138–150.
 115. Simmons GH, ed. *The Scintillation Camera*. The Society of Nuclear Medicine, 1988: 1–78.
 116. King MA, Glick SJ, Penney BC, Schwinger RB. Interactive visual optimization of SPECT pre-reconstruction filtering. *J Nucl Med* 1987; 28: 1192–1198.
 117. Ogawa K, Paek S, Nakajima M, Yuta S, Kubo A, Hashimoto S. Correction of collimator aperture using shift-variant deconvolution filter in gamma camera CT. In *Proceedings of SPIE Medical Imaging II: Image Processing, vol. 914*, 1988: 699–706.
 118. Lewitt RM, Edholm PR, Xia W. Fourier method for correction of depth-dependent collimator blurring. In *Proceedings SPIE Med Imag III: Image Processing, vol. 1092*, 1989: 232–243.
 119. Xia W, Lewitt RM, Edholm PR. Fourier correction for spatially variant collimator blurring in SPECT. *IEEE Trans Med Imag* 1995; 14: 100–115.
 120. Frey EC, Tsui BMW, Gullberg GT. Improved estimation of the detector response function for converging beam collimators. *Phys Med Biol* 1998; 43: 941–950.
 121. Lalush DS, Tsui BMW. Mean-Variance Analysis of block-iterative reconstruction algorithms modeling 3D detector response in SPECT. *IEEE Trans Nucl Sci* 1998; 45: 1280–1287.
 122. Yokoi T, Shinohara H, Onishi H. Performance evaluation of OSEM reconstruction algorithm incorporating three-dimensional distance-dependent resolution compensation for brain SPECT: A simulation study. *Ann Nucl Med* 2002; 16: 11–18.

123. Katu H, Ogawa K. An iterative correction method of image blurring by collimator aperture in single photon emission CT. *Trans IEICE* 1993; J76-D-II 2: 199–205.
124. Ogawa K, Katsu H. Iterative correction method for shift-variant blurring caused by collimator aperture in SPECT. *Ann Nucl Med* 1996; 10: 33–40.
125. Novikov RG. An inversion formula for the attenuated X-ray transformation. *Ark Mat* 2002; 40: 145–167.
126. Ishikawa A, Ogawa K. Implementation and evaluation of analytical attenuation correction for non-uniform attenuator. *Med Imag Tech* 2004; 22: 92–98.
127. Ishikawa A, Ogawa K. Reduction of streak artifacts in an analytical attenuation correction method for single photon emission CT. In *Proceedings of IASTED ASM 2004* (in press).
128. Kojima A, Tsuji A, Takaki Y, Tomiguchi S, Hara M, Matsumoto M, et al. Correction of scattered photons in Tc-99m imaging by means of a photopeak dual-energy window acquisition. *Ann Nucl Med* 1992; 6: 153–158.
129. Ishii M, Ogawa K, Nakahara T, Hashimoto J, Kubo A. Quantification of I-123 and Tc-99m in dual-isotope SPECT with an artificial neural network. *Med Imag Tech* 2004; 22: 155–163.